The effects of ice floe-floe interactions on pressure ridging in sea ice

A. Damsgaard[1,*], O. Sergienko[1], and A. Adcroft[1]

[1]Program in Atmospheric and Oceanic Sciences, Princeton University, Princeton, New Jersey, USA

[*]Now at Department of Geophysics, Stanford University, Stanford, California, USA

Key Points:

- Ice-floe interactions are simulated using particles connected with breakable bonds.
- Elasticity provides large resistance during compression of ice floes.
- Ridging becomes spatially localized due to weakening after floe compressive failure.

Corresponding author: A. Damsgaard, anders@adamsgaard.dk

Abstract

The mechanical interaction between ice floes in the polar sea-ice packs plays an important role in the state and predictibility of the ice cover. Using a Lagrangian-based numerical model we investigate the mechanics of sea ice floe-floe interactions. Our simulations show that elastic and reversible deformation offers significant resistance to compression before ice floes yield with brittle failure. When pressure ridges start to form, compressional strength dramatically decreases, implying thicker sea ice is not necessarily stronger compared to thinner ice. These effects are not accounted for in current sea-ice models that describe ice strength by thickness alone. As our results show, the observed transition in mechanical state during ridging initiation may lead to biases in simulated ridge building rates and sea-ice thickness. We propose a parameterization that describes failure mechanics from fracture toughness and Coulomb sliding, improving the representation of ridge building dynamics in particle-based and continuum sea-ice models.

Plain Language Summary

Considerable areas of the polar oceans are covered by sea ice, formed by frozen sea water. The extent and thickness of the ice pack influences local and regional ecology and climate. The thickness is in particular important for how resilient the ice is to warmer summers. Wind and ocean currents compress and shear the sea ice, and can break and stack ice bits into ridges over and under sea level. Current sea ice models assume that the ice becomes increasingly rigid as ridges of ice rubble grow. In this study, we model ice using a bonded particle model and show that ice becomes significantly weaker right after the onset of ridge building. We introduce a mathematical framework that allows these physics to be included in large-scale models.

1 Introduction

The presence of sea ice in the polar oceans has a profound effect on ocean-atmosphere interaction and global climate [e.g., *Curry et al.*, 1995; *Chiang and Bitz*, 2005; *Screen and Simmonds*, 2010]. The thickness of the sea-ice cover is a key factor controlling the summer sea-ice extent [e.g., *Lindsay et al.*, 2008; *Day et al.*, 2014; *Bushuk et al.*, 2017], but it remains difficult to observe remotely and predict accurately with numerical sea-ice models [e.g., *Haas*, 2003; *Holland et al.*, 2010; *Blanchard-Wrigglesworth et al.*, 2016]. In-

ternal stresses in sea ice floes and drag from ocean and atmosphere can build up ice in thick ridges under compression, or form leads of open water during extension that increase ocean-atmosphere energy exchange [e.g., *Parmerter and Coon*, 1973; *Thorndike et al.*, 1975; *Haas*, 2003; *Batrak and Müller*, 2018]. Ice ridging takes place when ice floes break into smaller pieces and create a chaotic and thick rubble [e.g., *Hopkins*, 1994]. The subaerial ice rubble produced by this process is called a *sail*, and the subaqueous part a *keel* [e.g., *Hopkins*, 1998]. Due to the difference in ice and water density, sea ice keels are deeper than their corresponding sails. Both keels and sails increase the form drag of the ice pack [*Tsamados et al.*, 2014].

In widely used large-scale continuum sea-ice models, the ice pack in each cell is described by thickness distribution functions [e.g., *Thorndike et al.*, 1975; *Flato and Hibler*, 1995; *Lipscomb et al.*, 2007; *Ungermann et al.*, 2017]. Ridge building modifies the thickness distribution, and is determined by the required increase in potential energy and associated frictional losses [*Coon*, 1974; *Pritchard*, 1975; *Rothrock*, 1975; *Hopkins et al.*, 1991; *Hopkins*, 1998]. The ice strength is parameterized to scale with ice thickness [e.g., *Hibler*, 1979; *Lipscomb et al.*, 2007]. However, established ridge building models may lead to biases in ice-thickness distribution, compared to observations [e.g., *Flato and Hibler*, 1995; *Amundrud et al.*, 2004; *Ungermann et al.*, 2017]. Furthermore, current ridging models based on the continuum assumption, are formulated for model-grid sizes exceeding by far individual ice-floe sizes. As a climate-model resolution increases, and potentially approaches size of large individual sea-ice floes, it becomes relevant to consider the physical basis for ridging on the ice-floe scale. Lagrangian particle-based sea ice models may be feasible alternatives to continuum models at fine resolutions [e.g., *Hopkins et al.*, 1991; *Gutfraind and Savage*, 1997; *Li et al.*, 2014; *Herman*, 2016; *Damsgaard et al.*, 2018], but still require model development for handling the multitude of involved physical phenomena.

Amundrud et al. [2004] presented a threshold for ridging per ice floe, based on the elastic buckling failure of an elastic plate (sea-ice floe) interacting with an elastic foundation (sea water). However, the threshold value does not account for ice plasticity that manifests itself in brittle failure under compression [e.g., *Coon*, 1974]. *Hopkins* [2004] first included ridging in a Lagrangian sea-ice model for the Arctic ocean. In this model compressional strength linearly relaxes after ridging failure, and the internal stress distribution is reset every 24 hours. However, the approach does not conform to physical principles

of elasticity, plastic failure and frictional sliding. Consequently, a new ridging parameterization is needed for particle-based sea-ice models, describing the stress and geometry evolution during compression (Fig. 1). *Flato and Hibler* [1995] argued that thickness distributions for intact and deformed ice should be considered separately. Here we show that the two states have drastically different mechanical properties.

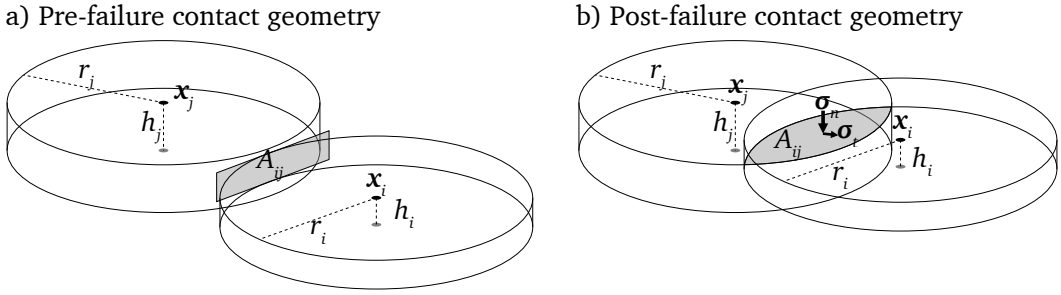

Figure 1. Particle-based sea-ice models are missing a parameterization describing how ice-floe pairs transition from an original, pre-failure state (a), to an actively ridging mode (b).

In this study, we analyze the mechanics of two simulated ice floes that undergo compressional strain. Based on these results, we derive a parameterization for larger-scale sea-ice models, and demonstrate how ridging mechanics influence larger-scale stress and strain distribution.

2 Compression experiments with two idealized ice floes

We start with a two-dimensional simulation of two ice floes constructed of many particles in a triangular packing connected by rigid bonds (Fig. 2I). These bonds transfer force and torque between particles elastically, and break according to a criterion derived from the elastic-plastic beam theory (Supplementary Text S1). Interactions between unbonded particles are elastic and frictional (according to the Coulomb friction law) [e.g., *Damsgaard et al.*, 2013, 2018]. We note that the bonded and unbonded elasticity is true material elasticity, that is different from the elastic term in elastic-viscous-plastic sea ice models where it is included for numerical efficiency [e.g., *Hunke*, 2001; *Lipscomb et al.*, 2007]. The momentum balance for ice-floe translation and rotation is explicitly integrated through time, and the simulated particle dynamics include the full physical range from elastic wave propagation to plastic rearrangement. The simulation domain is two-dimensional with one horizontal (x) and one vertical axis (z). Sea level is constant at $z = 0$ and the

water is motionless. Gravitational acceleration applies to all particles, and submerged volumes experience buoyant uplift and water drag. The outer edges of the ice floes are fixed horizontally, and can move up and down through a slip boundary condition. The ice floes are compressed with a constant velocity, and resultant stresses are monitored through time (insert figure in Fig. 2). Simulation parameters are listed in Table S1 in the supporting information. We vary the ice-floe thicknesses, ice-floe geometry, compressional velocity, and numerical resolution. Some experiments include instantaneous refreezing by bonding ice particles together upon contact. For comparison we also model compressive mechanics of a floating, elastic sheet, as well as purely elastic ice floes with unbreakable bonds. The mechanical properties are in all cases uniform throughout the domain.

2.1 Results

We divide the observed compressional deformation behavior into distinct stages of pre- and post-failure (Fig. 2). During the elastic pre-failure stage the thinner ice floe buckles upwards (Fig. 2II), and the ice floes experience large internal stresses. Buckling is common when slender or thin materials are subjected to a compressive stress, causing out-of-plane deflection and a reduction in elastic rigidity. Due to flotation, the ice-floe contact center is situated above the midpoint of the thicker ice floe. This geometric configuration creates a rotational moment at the floe-floe interface that bends the thinner ice floe upwards. During peak stress, yield failure occurs in the zone of maximum curvature and tensile stress located at the top of the thinner ice floe (Fig. 2II). In the post-failure state the ice floes break into many pieces creating a disorganized pressure ridge (Fig. 2III). Contact forces between ice bits are caused by gravity and buoyancy, and further compression is limited by Coulomb frictional sliding that leads to increase in potential energy. The observed behavior is independent of the model numerical resolution (Fig. S1). Experiments with instantaneous refreezing do not show different peak stress values, but display larger compressive strength in the post-failure state as the ice-rubble quickly gains cohesion (Fig. S2). However, the structural rigidity is still much lower than the intact, pre-failure state. We do note that strength and geometrical variations in the third dimension are likely to provide more a gradual yield failure across space, but this is outside of our current simulation capabilities.

Simulations of an elastic sheet instead of two discrete elastic-plastic ice floes, reproduce analytical buckling solution (Fig. 3, *Amundrud et al.* [2004]). However, our results

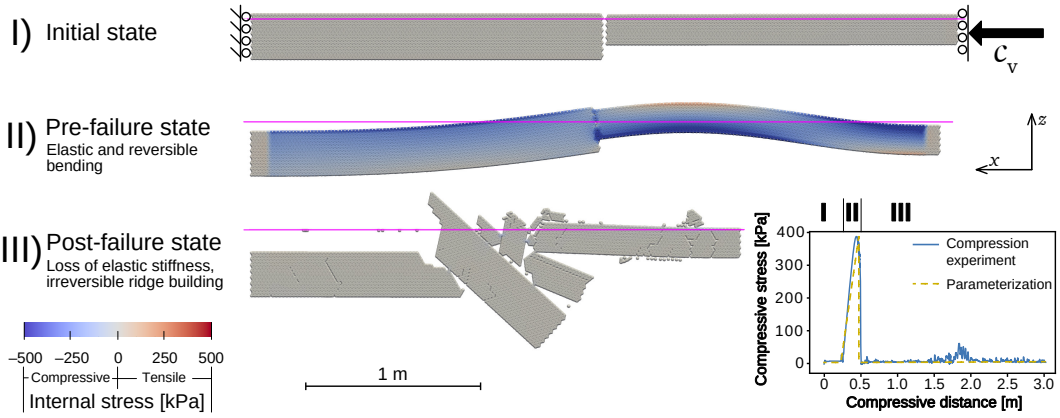

Figure 2. Simulated interaction between two elastic-plastic ice floes, seen from the side. We simulate the mechanical response under a constant compressive strain rate with velocity c_v. Compression causes first-order buckling (II) that can evolve to ridging in the case of brittle failure (III). Time and compressive strain increase downwards, and magenta horizontal lines denote sea level. The insert figure shows observed compressive stress during compression and stresses modeled with our parameterization.

show that the compressive strength of an elastic sheet is an overestimation of the ice rigidity compared to simulations of two discrete and elastic(-plastic) ice floes. We propose a first-principles formulation for the maximum compressive strength in sea ice models that fits our observations, $N_{\max} = K_{\mathrm{Ic}} h_{\min}^{3/2} A^{-1}$, where $N_{\max}$ is the maximum compressive stress, K_{Ic} is the fracture toughness of the sea ice, $h_{\min}$ is the thinnest ice thickness participating in the ridging, and A is the transverse contact area (Fig. 1a). The resultant stress-strain model for particle sea-ice models is listed in Supplementary Information S2.1 to S2.3. A commonly used value for sea-ice fracture toughness is 1.285×10^6 Pa $\mathrm{m}^{1/2}$ [*Hopkins*, 2004]. The relationship implies that thinner ice floes in a multi-thickness assemblage are likely to ridge before thicker floes. However, the relationship between ice thickness and ridging participation is not linear, as is commonly assumed [e.g., *Hibler*, 1979; *Lipscomb et al.*, 2007]. Stresses during post-failure sliding are elastic and limited by Coulomb friction on the contact surface, and can be parameterized from the ice-floe shape and frictional properties (SI Eq. 10 and 11).

3 Bulk dynamics with ridging parameterization

To investigate the performance of the formulation for the maximum compressive strength described above, we implement it in a larger-scale particle sea-ice model. The

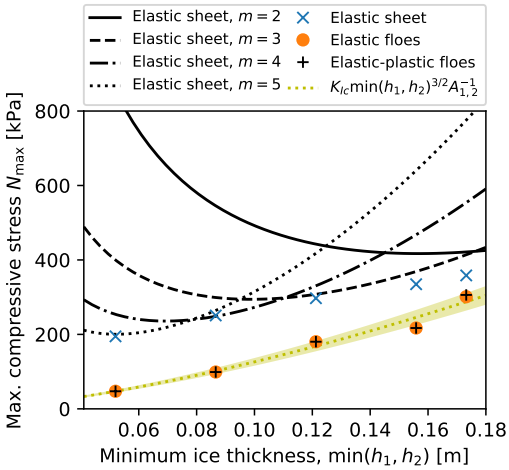

Figure 3. Comparison of buckling stresses in our elastic-plastic ice floe simulations (cross symbols) with analytical derivations for elastic plates floating on an elastic ocean [Eq. 6 in *Amundrud et al.*, 2004]. The bending mode in the analytical model is denoted m, and the simulation compressive velocity is c_v.

model is two-dimensional and oriented in plan view at the sea surface. Each ice floe is simulated with a single Lagrangian particle with discrete-element contact mechanics [e.g., *Gutfraind and Savage*, 1997; *Hopkins*, 2004; *Herman*, 2016; *Damsgaard et al.*, 2018]. Different from discrete-element methods, the ridging parameterization limits the compressive stresses between particles. The contacts switch to post-failure mode if peak compressive stresses are reached. Full details can be found in Supplementary Text S2. Post-failure compressive stress is parameterized as a function of frictional resistance along the sliding interface (Fig. 1b). The observed non-monotonic stress-strain behavior is in contrast to the conventional approach where thickness governs compressive sea-ice strength alone, and no distinction is made between intact and actively ridging ice [e.g., *Rothrock*, 1975; *Hibler*, 1979]. We first compare the ridging parameterization to the detailed elastic-plastic compressional experiments (insert figure in Fig. 2). The proposed parameterization captures the stress transition and main low-frequency dynamics in the two-floe elastic-plastic experiment.

To assess the influence on bulk assemblage properties under uniaxial compression, we vary fracture toughness (K_{Ic}) from 1.285×10^5 Pa m$^{1/2}$ to 1.285×10^7 Pa m$^{1/2}$ (Fig. 4). Cylindrical ice floes are randomly generated with diameters between 40 and 200 m and a uniform thickness of 1 m. Elastic and frictional parameters are identical to the two-floe

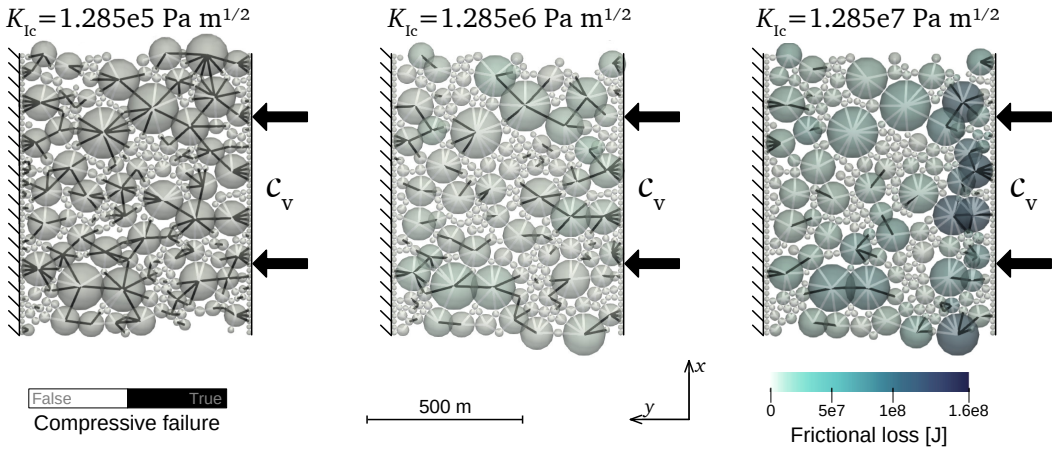

Figure 4. Uniaxial compression experiments at a compressive strain of $\epsilon_c = 0.45$. Ice floes are colored according to their thermal energy increase contributed by pre and post-failure contact sliding. Contacts between ice floes are marked by straight lines. White lines denote contacts in the pre-failure state, while black lines denote failure and active ridging. K_{Ic} is the applied fracture toughness value for each experiment, and c_v is the compressive velocity.

compression experiment (Table S1). The right boundary $(-y)$ of each run is moved at a constant rate towards the left (Fig. 4). The left boundary $(+y)$ is fixed, and the top and bottom (x) boundaries are periodic. Figure 4 shows the deformation behavior during uniaxial compression. With low fracture toughnesses ($K_{Ic} = 1.285 \times 10^5$ Pa m$^{1/2}$) the deformation is distributed and the majority of contacts ridge. With higher fracture toughnesses, less contacts ridge and deformation is more localized, as evident from the distribution of frictional energy (ice-floe colors in Fig. 4). The bulk compressive strength of the ice-floe assemblage is heavily influenced by the choice of fracture toughness (Fig. S3). Low fracture toughness values cause a low bulk compressive stress as ice floes soon reach the weak post-failure state. With higher fracture toughnesses the bulk assemblage strengthens, and individual ridging events exert significant decreases in the bulk compressive stress. Failure between ice floes cause stick-slip dynamics due to the rapid decreases in compressive stress (Fig. S3 and Supplementary Movies 1 and 2). Similar to axial compression, the fracture toughness value also dictates strain distribution during simple shear (Fig. S4). Low fracture toughnesses result in widespread ridging, while ridging localizes at the boundaries with increasing fracture toughness.

4 Discussion and Conclusions

Sea ice ridging increases ice-pack thickness, and plays an important role in the formation of multi-year ice. Present sea-ice models use an assumption that compressive stress monotonically increases during compression. However, results of a high-resolution Lagrangian model used in this study show that the deformation is characterized by two distinct stages. One is reversible elastic deformation, and the other one is irreversible brittle failure and ridge building. When ridging is initiated the compressive stress decreases by more than two orders of magnitude. The low compressional failure during ridge building is controlled by Coulomb sliding, buoyancy, and potential energy increase. The transient mechanical interections are in direct contrast to current sea-ice models that determine compressive stress from ice thickness alone, without distinguising between ridging and non-ridging mechanics. Based on results of the Lagrangian-particle model simulations we propose to parameterize the observed behavior based on the first principles of fracture toughness and Coulomb sliding, suitable for simulating ridging in particle-based sea-ice models. Elastic strength before failure depends on the ice thickness to a power of 3/2. In assemblages of many ice floes the mechanical transition and associated weakening causes stick-slip dynamics and strain localization, particularly with higher fracture toughness values. The proposed parameterization of elastic deformation and brittle failure effects on strength can be implemented in large-scale particle and continuum based sea-ice models. The parameterization potentially improves formation and dynamics of damaged zones, and consequently fidelity in representation of sea-ice state in climate models.

Acknowledgments

This work was supported by ExxonMobil through its membership in the Princeton E-filliates Partnership of the Andlinger Center for Energy and the Environment. The authors declare no financial conflicts of interests. AA and OS are supported by awards NA13OAR439 and NA18OAR4320123 from the National Oceanic and Atmospheric Administration, US Department of Commerce. The statements, findings, conclusions and recommendations are those of the authors and do not necessarily reflect the views of the National Oceanic and Atmospheric Administration, or the US Department of Commerce. Source code for the numerical modeling is available at doi:10.5281/zenodo.3471354.

References

Amundrud, T. L., H. Melling, and R. G. Ingram (2004), Geometrical constraints on the evolution of ridged sea ice, *J. Geophys. Res.*, *109*(C6), doi:10.1029/2003jc002251.

Batrak, Y., and M. Müller (2018), Atmospheric response to kilometer-scale changes in sea ice concentration within the marginal ice zone, *Geophys. Res. Lett.*, *45*(13), 6702–6709, doi:10.1029/2018gl078295.

Blanchard-Wrigglesworth, E., A. Barthélemy, M. Chevallier, R. Cullather, N. Fučkar, F. Massonnet, P. Posey, W. Wang, J. Zhang, C. Ardilouze, C. M. Bitz, G. Vernieres, A. Wallcraft, and M. Wang (2016), Multi-model seasonal forecast of Arctic sea-ice: forecast uncertainty at pan-Arctic and regional scales, *Clim. Dyn.*, *49*(4), 1399–1410, doi:10.1007/s00382-016-3388-9.

Bushuk, M., R. Msadek, M. Winton, G. A. Vecchi, R. Gudgel, A. Rosati, and X. Yang (2017), Skillful regional prediction of Arctic sea ice on seasonal timescales, *Geophys. Res. Lett.*, *44*(10), 4953–4964, doi:10.1002/2017gl073155.

Chiang, J. C. H., and C. M. Bitz (2005), Influence of high latitude ice cover on the marine Intertropical Convergence Zone, *Clim. Dyn.*, *25*(5), 477–496, doi:10.1007/s00382-005-0040-5.

Coon, M. (1974), Mechanical behavior of compacted Arctic ice floes, *J. Petr. Tech.*, *26*(04), 466–470, doi:10.2118/3956-pa.

Cundall, P. A., and O. D. L. Strack (1979), A discrete numerical model for granular assemblies, *Géotechnique*, *29*, 47–65, doi:10.1680/geot.1979.29.1.47.

Curry, J. A., J. L. Schramm, and E. E. Ebert (1995), Sea ice-albedo climate feedback mechanism, *J. Climate*, *8*(2), 240–247, doi:10.1175/1520-0442(1995)008<0240:siacfm>2.0.co;2.

Damsgaard, A., D. L. Egholm, J. A. Piotrowski, S. Tulaczyk, N. K. Larsen, and K. Tylmann (2013), Discrete element modeling of subglacial sediment deformation, *J. Geophys. Res. Earth Surf.*, *118*, 2230–2242, doi:10.1002/2013JF002830.

Damsgaard, A. (2018), Granular.jl: Julia package for granular dynamics simulation, doi:10.5281/zenodo.1165989.

Damsgaard, A., A. Adcroft, and O. Sergienko (2018), Application of discrete-element methods to approximate sea-ice dynamics, *J. Adv. Model. Earth Sys.*, *10*(9), 2228–2244, doi:10.1029/2018MS001299.

256 Day, J. J., E. Hawkins, and S. Tietsche (2014), Will Arctic sea ice thickness initializa-
257 tion improve seasonal forecast skill?, *Geophys. Res. Lett.*, *41*(21), 7566–7575, doi:
258 10.1002/2014gl061694.

259 Flato, G. M., and W. D. Hibler (1995), Ridging and strength in modeling the thickness
260 distribution of Arctic sea ice, *J. Geophys. Res.*, *100*(C9), 18,611, doi:10.1029/95jc02091.

261 Gutfraind, R., and S. B. Savage (1997), Marginal ice zone rheology: Comparison of re-
262 sults from continuum-plastic models and discrete-particle simulations, *J. Geophys. Res.:*
263 *Oceans*, *102*(C6), 12,647–12,661, doi:10.1029/97jc00124.

264 Haas, C. (2003), Dynamics versus thermodynamics: The sea ice thickness distribution, in
265 *Sea Ice*, pp. 82–111, Blackwell Science Ltd, doi:10.1002/9780470757161.ch3.

266 Herman, A. (2016), Discrete-element bonded-particle sea ice model DESIgn, version 1.3a
267 – model description and implementation, *Geosci. Mod. Dev.*, *9*(3), 1219–1241, doi:
268 10.5194/gmd-9-1219-2016.

269 Hibler, W. D. (1979), A dynamic thermodynamic sea ice model, *J. Phys. Oceanogr.*, *9*(4),
270 815–846, doi:10.1175/1520-0485(1979)009<0815:adtsim>2.0.co;2.

271 Holland, M. M., M. C. Serreze, and J. Stroeve (2010), The sea ice mass budget of the
272 arctic and its future change as simulated by coupled climate models, *Clim. Dyn.*, *34*(2-
273 3), 185–200, doi:10.1007/s00382-008-0493-4.

274 Hopkins, M. A. (1994), On the ridging of intact lead ice, *J. Geophys. Res.*, *99*(C8),
275 16,351, doi:10.1029/94jc00996.

276 Hopkins, M. A. (1998), Four stages of pressure ridging, *J. Geophys. Res.: Oceans*,
277 *103*(C10), 21,883–21,891, doi:10.1029/98jc01257.

278 Hopkins, M. A. (2004), A discrete element Lagrangian sea ice model, *Eng. Comput.*,
279 *21*(2/3/4), 409–421, doi:10.1108/02644400410519857.

280 Hopkins, M. A., W. D. Hibler, and G. M. Flato (1991), On the numerical simulation of
281 the sea ice ridging process, *J. Geophys. Res.*, *96*(C3), 4809, doi:10.1029/90jc02375.

282 Hunke, E. C. (2001), Viscous–plastic sea ice dynamics with the EVP model: Linearization
283 issues, *J. Comput. Phys.*, *170*(1), 18–38, doi:10.1006/jcph.2001.6710.

284 Li, B., H. Li, Y. Liu, A. Wang, and S. Ji (2014), A modified discrete element model for
285 sea ice dynamics, *Acta Oceanol. Sin.*, *33*(1), 56–63, doi:10.1007/s13131-014-0428-3.

286 Lindsay, R. W., J. Zhang, A. J. Schweiger, and M. A. Steele (2008), Seasonal pre-
287 dictions of ice extent in the Arctic ocean, *J. Geophys. Res.: Oceans*, *113*(C2), doi:
288 10.1029/2007jc004259.

Lipscomb, W. H., E. C. Hunke, W. Maslowski, and J. Jakacki (2007), Ridging, strength, and stability in high-resolution sea ice models, *J. Geophys. Res.*, *112*(C3), doi: 10.1029/2005jc003355.

Parmerter, R., and M. Coon (1973), On the mechanics of pressure ridge formation in sea ice, in *Offshore Technology Conference*, Offshore Technology Conference, doi: 10.4043/1810-ms.

Potyondy, D. O., and P. A. Cundall (2004), A bonded-particle model for rock, *Int. J. Rock Mech. Min.*, *41*(8), 1329–1364.

Pritchard, R. S. (1975), An elastic-plastic constitutive law for sea ice, *J. Appl. Mech.*, *42*(2), 379, doi:10.1115/1.3423585.

Rothrock, D. A. (1975), The energetics of the plastic deformation of pack ice by ridging, *J. Geophys. Res.*, *80*(33), 4514–4519, doi:10.1029/jc080i033p04514.

Screen, J. A., and I. Simmonds (2010), The central role of diminishing sea ice in recent Arctic temperature amplification, *Nature*, *464*(7293), 1334–1337, doi: 10.1038/nature09051.

Thorndike, A. S., D. A. Rothrock, G. A. Maykut, and R. Colony (1975), The thickness distribution of sea ice, *J. Geophys. Res.*, *80*(33), 4501–4513, doi: 10.1029/jc080i033p04501.

Tsamados, M., D. L. Feltham, D. Schroeder, D. Flocco, S. L. Farrell, N. Kurtz, S. W. Laxon, and S. Bacon (2014), Impact of variable atmospheric and oceanic form drag on simulations of arctic sea ice, *J. Phys. Ocean.*, *44*(5), 1329–1353, doi:10.1175/jpo-d-13-0215.1.

Ungermann, M., L. B. Tremblay, T. Martin, and M. Losch (2017), Impact of the ice strength formulation on the performance of sa sea ice thickness distribution model in the arctic, *J. Geophys. Res.: Oceans*, *122*, 2090–2107, doi:10.1002/2016JC012128.